International Journal of Solids and Structures 221 (2021) 2–17

Contents lists available at ScienceDirect

International Journal of Solids and Structures

journal homepage: www.elsevier.com/locate/ijsolstr

Buckling and collapse of pseudoelastic NiTi tubes under bending

Karlos Kazinakis, Stelios Kyriakides *, Dongjie Jiang, Nathan J. Bechle, Chad M. Landis

Research Center for Mechanics of Solids, Structures & Materials, ASE, The University of Texas at Austin, Austin, TX 78712, USA

ARTICLE INFO

Article history:
Received 7 July 2019
Received in revised form 10 December 2019
Accepted 28 December 2019
Available online 30 December 2019

Keywords:
Bending of NiTi Tubes
Pseudoelasticity
Inhomogeneous deformation
Buckling

ABSTRACT

Pseudoelastic NiTi structural components have been shown to exhibit tension/compression asymmetry. Under tension, phase transformation induces localized strains of nearly 7% that spread under nearly constant stress, while under compression the transformation leads to hardening at significantly higher stress, the strain is smaller and grows homogeneously. Bending of tubes ovalizes their cross-section, a nonlinearity that reduces the bending rigidity and precipitates instabilities that can lead to collapse. This paper uses experiment and analysis to examine the interaction of these geometric nonlinearities with the complex material behavior of pseudoelastic NiTi tubes of moderate diameter-to-thickness ratios under bending. An experiment on a tube with a diameter-to-thickness ratio of 18.7 shows that transformation causes the nucleation of several dispersed high strain banded patterns of martensite on the tensioned side. The zone where the bands coalesce into intersecting diamonds undergoes excessive local ovalization causing buckling and collapse at a relatively low overall tube curvature. The bending experiment is simulated with a finite element model coupled with a custom constitutive model of pseudoelastic NiTi that allows for plastic deformation of the martensitic phase. The analysis reproduces the moment-end rotation response, and the nucleation and evolution of the high strain diamond shaped patterns. Zones that develop such patterns exhibit accelerated growth of ovalization that degrades the local bending rigidity. In the presence of small geometric imperfections this degradation evolves into a buckle in the form of diffuse local ovalization that precipitates collapse that can negate the recoverable property of NiTi. Parametric studies show that as the tube D/t increases, the interaction between the material and geometric nonlinearities becomes stronger making buckling more imperfection sensitive.

© 2019 Elsevier Ltd. All rights reserved.

1. Introduction

Under stress, nearly equiatomic NiTi transforms from an austenitic to a martensitic phase at room temperature levels. The change in phase results in deformation of the order of 6–8% that is recoverable on unloading, a remarkable phenomenon known as pseudoelasticity. Under tensile stress states, transformation results in inhomogeneous deformation (e.g., see Shaw and Kyriakides, 1995, 1997; Li and Sun, 2002; Abeyaratne and Knowles, 2006; Bechle and Kyriakides, 2014, 2016a,b; Reedlunn et al., 2014; Watkins et al., 2018). Under compression the transformation requires significantly higher stress, results in lower strain, and deformation is essentially homogeneous (e.g., Jacobus et al., 1996; Gall and Sehitoglu, 1999; Gall et al., 1999; Mao et al., 2010; Bechle and Kyriakides, 2014; Reedlunn et al., 2014; Watkins et al., 2018). In pure bending experiments on NiTi tubes, this material asymmetry manifests in the coexistence of two curvature regimes with diamond-shaped higher strain patterns of martensite developing on the tensioned side. Two curvatures exist also on unloading accompanied by the progressive erasure of the diamond patterns.

This complex bending behavior was reproduced in Jiang et al. (2017b) using a finite element analysis coupled with a constitutive model of pseudoelastic behavior of NiTi implemented into a custom material subroutine in ABAQUS (see also Jiang et al., 2016a, b). The tension/compression asymmetry is captured by incorporating both the tensile and compressive responses of the material in the model. The material instability exhibited in tension is simulated by adding softening over the extents of the inhomogeneous branches of the measured stress-elongation response.

The bending experiments reported in Bechle and Kyriakides (2014) and analyzed in Jiang et al. (2017b) involved relatively thick-walled tubes with $D/t \approx 8.5$. However, NiTi tubes used in catheters and other applications can be significantly thinner, so the bending induced ovalization of the cross section becomes increasingly more prominent in their response and stability. The present work uses experiment and analysis to investigate how the transformation induced material nonlinearities interact

*Corresponding author.
E-mail address: skk@mail.utexas.edu (S. Kyriakides).

https://doi.org/10.1016/j.ijsolstr.2019.12.017
0020-7683/© 2019 Elsevier Ltd. All rights reserved.

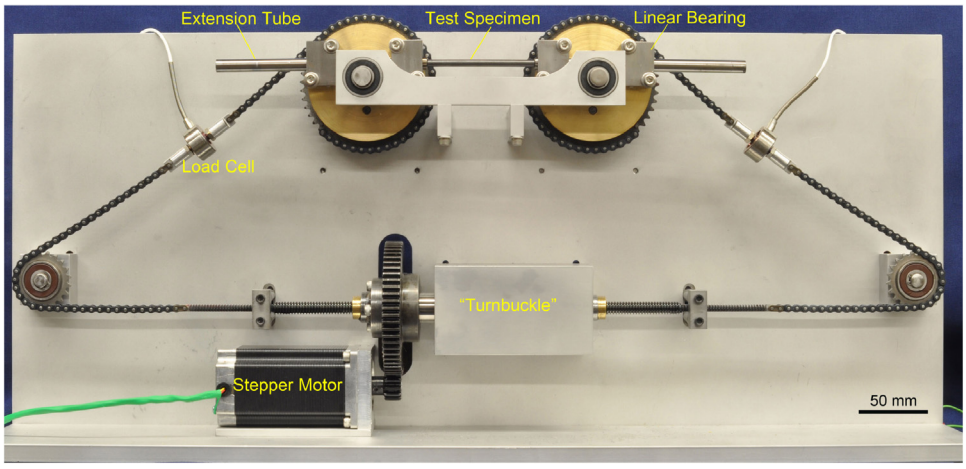

Fig. 1. Miniature bending device used to conduct pure bending of NiTi tubes (Bechle and Kyriakides, 2014).

with geometric nonlinearities and result in limit states of the structure.

Pure bending experiments on pseudoelastic NiTi tubes with $D/t \approx 18.7$ reported in the next section demonstrate that the interaction of material and geometric nonlinearities leads to local buckling, collapse, and eventually fracture of a pseudoelastic NiTi tube. The finite element model of Jiang et al. (2017b) is extended to address buckling and used to simulate the experiment. The model is subsequently used to study the sensitivity of buckling to geometric imperfections and to the tube D/t. The study is completed with a sensitivity analysis of the stability of a base case to key parameters of the constitutive model.

2. Experimental

Bending experiments on pseudoelastic NiTi tubes with a diameter of 5.1 mm (0.20 in.) and $D/t \approx 18.7$ were performed in the four point bending device shown in Fig. 1 (Bechle and Kyriakides, 2014). Briefly, the device consists of two free-spinning sprockets mounted on a stiff support structure 165 mm (6.5 in.) apart. The sprockets are rotated by contracting the length of chains that run around them through a "turnbuckle" operated by a stepper motor. The ends of the tubes tested are mounted into case-hardened and ground-finished 9.5 mm (0.375 in.) extension tubes leaving a test section 76 mm (3.0 in.) long. The extension tubes engage two low-friction linear bearings mounted on each sprocket. Rotation of the sprockets results in four-point bending of the specimen, while the linear bearings allow the extension rods to slide inwards to accommodate the required change in length. The rotations of the sprockets are monitored by rotary transducers, and the moment is established from the tension in the chains monitored by inline load cells. The tests were performed at a slow rotation rate resulting in bending strain rates of about 10^{-5} s^{-1} (for more details on bending experiments on SMA tubes see Bechle and Kyriakides, 2014).

The moment and end rotations of the specimen were recorded through a LabVIEW based data acquisition system. An infrared camera was employed to ensure that the temperature in the specimen was kept constant, and a high resolution DSLR camera was used to capture full-field images of the deforming tube. In addition, a black speckle pattern was spay-painted on the specimen over a white undercoat to facilitate the capture of the full-field deformation of the tube using digital image correlation (DIC).

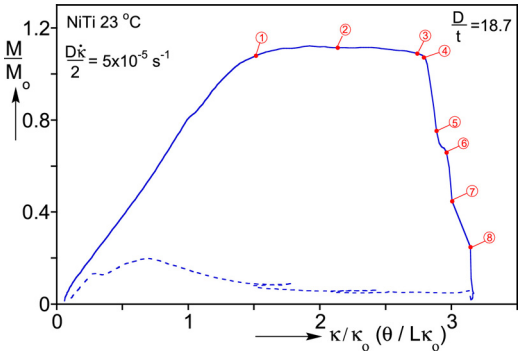

Fig. 2. Moment-end rotation response recorded in an isothermal pure bending experiment on a NiTi tube with $D/t = 18.7$ at 23 °C (solid line; the dashed line represents the recovery as the rotation is reduced).

We present results from an isothermal experiment at 23 °C. The main parameters of the tube tested are listed in Table 1. Fig. 2 shows the normalized bending moment-end rotation $(M/M_o - \bar{\theta}L/\kappa_o)$ response, where $\bar{\theta}$ is the average of the rotations recorded at each end. The normalizing parameters are:

$$M_o = \sigma_{PM} D_o^2 t \text{ and } \kappa_o = 2\varepsilon_o/D, \quad (1)$$

where D is the diameter of the tube, t is its wall thickness, $D_o = D - t$, $2L$ is the length of the test section, σ_{PM} is the average value of the austenite-to-martensite transformation stress in tension, and ε_o is the strain at first nucleation of martensite in tension.

When the tube bends uniformly, the curvature is $\kappa = \bar{\theta}/L$. Fig. 3 (a) shows a select number of images of the deforming specimen with axial strain contours extracted from 2-D DIC superimposed. They correspond to the stations marked on the response in Fig. 2 with solid bullets. Fig. 3(b) shows additional photographic images

Table 1
Main geometric and material parameters of the tube tested.

T°C	D mm (in)	t mm (in)	2 L mm (in)	σ_{PM} MPa (ksi)	ε_o
23	5.13 (0.202)	0.254 (0.010)	76.0 (3.0)	460 (66.7)	0.0106

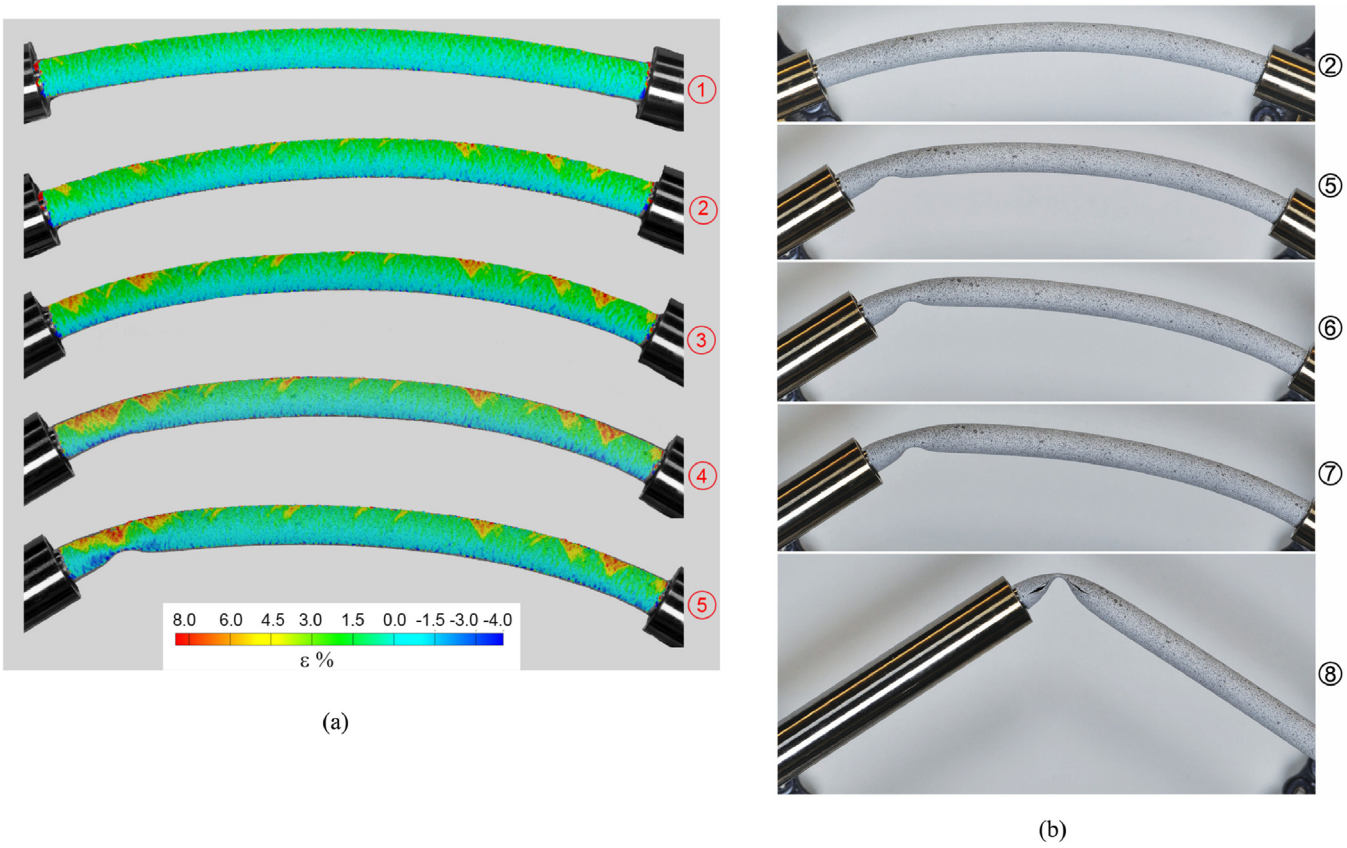

Fig. 3. Bending configurations corresponding to the numbered bullets on the experimental response in Fig. 2 that show the evolution of a local buckle that leads to collapse and fracture. (a) Localized deformation patterns captured by DIC– $\varepsilon \equiv$ axial strain–, and (b) photographic images.

without strain contours mainly from the descending part of the response.

Initially, the material is in the austenitic phase and the tube bends uniformly tracing a nearly linear response with the corresponding bending rigidity. Bending progressively ovalizes the tube cross section, which combined with some early, dispersed material transformation results in a gradual reduction in bending rigidity commencing at a curvature of about $1.20\kappa_o$ (Brazier, 1927; Kyriakides and Ju, 1992; Ju and Kyriakdes, 1992). In image ① at a curvature of $1.51\kappa_o$, the tube is uniformly bent, but the first islands of localized deformation have emerged on the tensioned side. Further bending results in a progressive initiation of transformed martensite, mostly in the form of inclined bands such as those observed in image ② at a curvature of $2.14\kappa_o$. The tendency of transformation bands getting organized into diamond shapes is now observed, such as those reported in Bechle and Kyriakides (2014), Reedlunn et al., (2014), and Jiang et al., (2017b). The specimen maintains its circular arc shape, while the moment remains essentially unchanged. In image ③ at a curvature of $2.74\kappa_o$, more bands have nucleated so that the previous patterns have developed into diamonds, and additional nucleation sites have appeared. The deformation patterns have strain levels that exceed 6% and tend to be rather randomly distributed along the extrado. The tube in this configuration remains uniformly bent but the moment starts to decrease, indicating the onset of structural instability. At the slightly higher curvature of station ④, a third diamond pattern has appeared between the two adjacent diamonds close to the left end. Simultaneously, a buckle in the form of diffused localized ovalization extending over about two tube diameters has appeared on the compressed side opposite to the three diamonds, and the moment has dropped further. The tube is now collapsing rather precipitously, and in the next image captured, ⑤, the moment has dropped by 25% from its plateau level, and the local buckle has deepened significantly. The unloading leads to some changes to the diamonds directly above the buckle, but because the curvature of the rest of the tube remains essentially unchanged, the patterns in this section remain the same. Beyond this point the moment drops in jumps. In the images corresponding to stations ⑥ and ⑦ the buckle becomes deeper, further reducing the local rigidity leading to local folding and unloading over the rest of the tube. The strain in the local fold has exceeded the strength of the material causing it to fracture as shown in image ⑧. Concurrently, the unaffected part of the tube has returned to the straight configuration. Included with a dashed line is the path followed as the rotation of the sprockets is reduced. The specimen returns to the straight configuration but remains locally cracked.

In summary, the higher strains associated with localized phase transformation interact with the bending induced ovalization to reduce the local bending rigidity causing the tube to buckle and collapse. The strains in the buckled zone cause yielding and further reduction in the local bending rigidity, which in turn causes flattening and fracture.

3. Analysis

An analysis, broadly along the lines of that in Jiang et al. (2017b), is used to first simulate the bending behavior of the $D/t =$ 18.7 NiTi tube used in the experiment, with particular emphasis on the observed buckling and collapse; and second to study the instability parametrically. A finite element model of tube bending is developed in the nonlinear code ABAQUS. It incorporates a custom constitutive model as a UMAT that captures the material non-

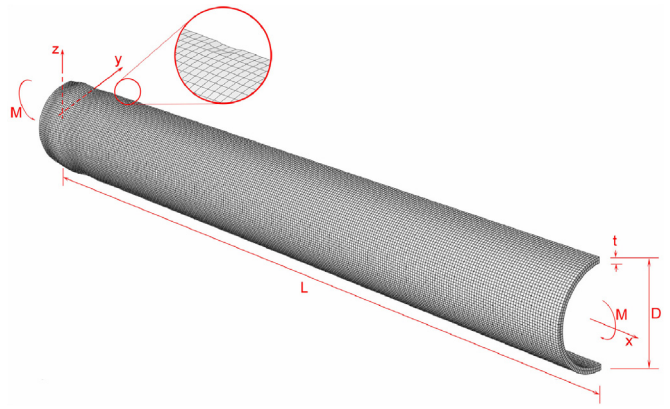

Fig. 4. Geometry of the finite element model used in the analysis with two thickness depressions and an axisymmetric imperfection near the $x = 0$ symmetry plane.

linearities including the tension/compression asymmetry of pseudoelastic SMAs, and allows for plastic deformations of the martensitic phase. The structural and constitutive models are outlined below.

3.1. Finite element model

Bending is simulated numerically using a finite element model developed in ABAQUS/Standard. A tube of diameter D, wall thickness t, and length $2L$ is loaded under pure bending. Symmetry about the plane of bending, $x-z$, and about the $y-z$ plane at the mid-span, limits consideration to one-quarter of the structure as shown in Fig. 4 (see Hallai and Kyriakides, 2011b; Jiang et al., 2017b). In order to initiate the structural instability in a consistent manner, a small axisymmetric geometric imperfection is introduced at the mid-span defined by

$$\frac{\bar{w}}{R} = a\cos\frac{\pi x}{\lambda}\exp\left[-\beta\left(\frac{x}{L}\right)^2\right], \tag{2}$$

where 2λ ($= 1.184R$) is the wavelength of the elastic buckling mode under axial compression, and β is a decay parameter assigned the value of 100. In addition, in order to maximize the interaction between the expected structural instability with the transformation induced localized strain two small thickness depressions are introduced at the plane of symmetry a distance D from the mid-span as shown in Fig. 4.

The structure is discretized using the 8-node linear brick incompatible elements C3D8I (e.g., see Hallai and Kyriakides, 2011b; Jiang et al., 2017a,b); incompatible elements ensure continuity of displacements but allow variations in the strain gradients within them). A mesh with nearly cubic hexahedral elements is adopted with 2 elements across the thickness, 66 around the half circumference, and 280 along the half-length for a total about 650,000 degrees of freedom. The tube is bent by prescribing the angle of rotation, θ_L, at $x = L$, where the cross-section is constrained to remain planar, while it is free to ovalize, by imposing the multipoint constraint

$$\tan\theta_L = \frac{x_{ref} - x_i}{z_{ref} - z_i}. \tag{3}$$

of the reference point at the initial center of the cross-section.

The moment about the y-axis is evaluated at $x = 0$ from

$$M = 2\sum_i z_i F_{xi}, \tag{4}$$

where F_{xi} is the axial force on the ith node of the cross-section, and z_i is its distance from the x-y plane.

3.2. Constitutive model

The constitutive model adopted is based on that presented in Jiang et al. (2016b) and Jiang and Landis (2016) and used in the preceding study of bending of pseudoelastic tubes in Jiang et al. (2017b). In the post-buckling regime the tubes analyzed here can undergo plastic deformations, and as such the model includes yielding of the martensite once a certain stress level is reached. Thus the strain increment is decomposed into elastic, transformation, and plastic ones

$$\dot{\varepsilon}_{ij} = \dot{\varepsilon}^e_{ij} + \dot{\varepsilon}^t_{ij} + \dot{\varepsilon}^p_{ij}. \tag{5}$$

Elastic deformations are linear and isotropic with constant (E, ν), which are assumed to be common to both phases. The elastic deformation is enclosed in a transformation surface that follows kinematic hardening

$$\Phi^t = \frac{3}{2}\left(s_{ij} - s^B_{ij}\right)\left(s_{ij} - s^B_{ij}\right) - \sigma_o^2 = 0 \tag{6}$$

where s^B_{ij} represents the deviatoric back stress. Plastic deformations obey isotropic hardening represented by the yield function

$$\Phi^p = \frac{3}{2}s_{ij}s_{ij} - \sigma_y^2 = 0. \tag{7}$$

The transformation and plastic strain increments obey normality through the following flow rules

$$\dot{\varepsilon}^t_{ij} = \Lambda^t\left(s_{ij} - s^B_{ij}\right), \quad \Lambda^t > 0 \tag{8}$$

and

$$\dot{\varepsilon}^p_{ij} = \Lambda^p s_{ij}, \quad \Lambda^p > 0. \tag{9}$$

The back stress is related to the transformation strain through a potential as follows

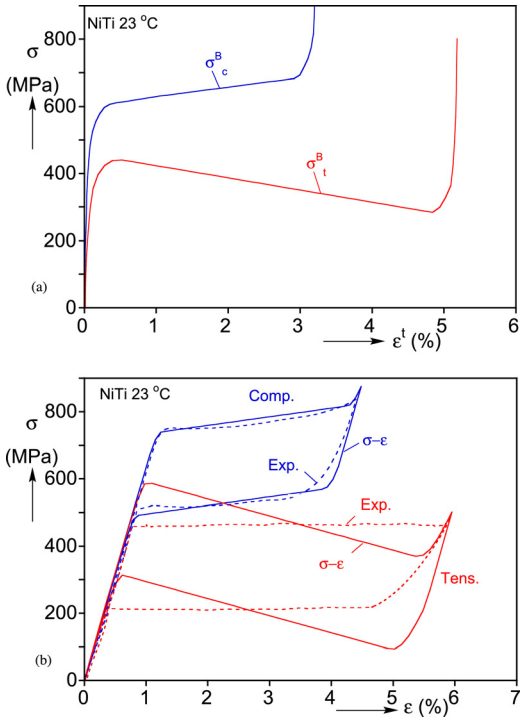

Fig. 5. (a) The adopted back stress-transformation strain responses in tension and compression. (b) Comparison of the resultant uniaxial tensile and compressive stress-strain responses to the measured ones.

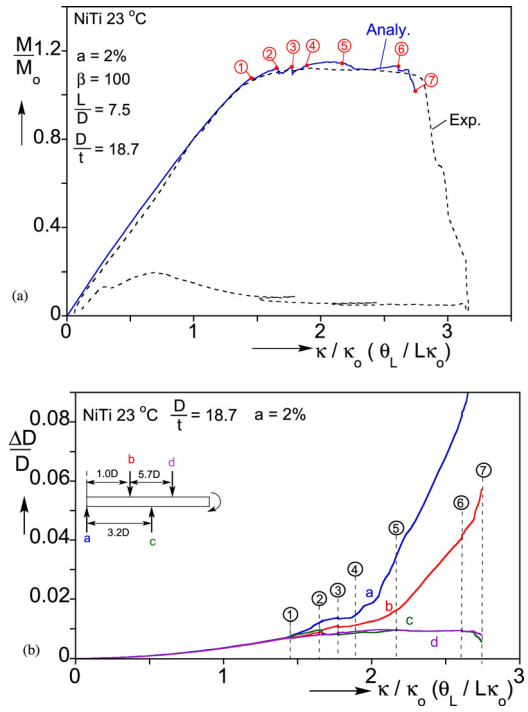

Fig. 6. (a) Calculated moment-end rotation response for tube with $D/t = 18.7$ for imperfection amplitude of $0.02R$ together with the measured response. (b) Induced change in diameter in the plane of bending at four sites identified in configuration ④ in Fig. 7.

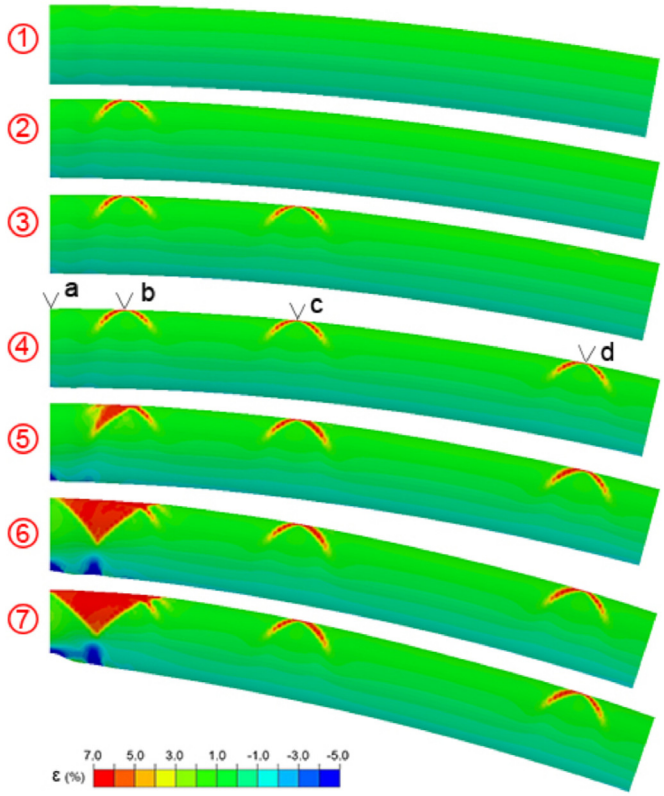

Fig. 7. Sequence of deformed configurations with axial strain contours superimposed corresponding to the numbered bullets on the calculated response in Fig. 6 (a).

$$\sigma_{ij}^{B} = \frac{\partial \psi^{t}}{\partial \varepsilon_{ij}^{t}}. \tag{10}$$

The tension/compression asymmetry exhibited by this material is introduced by expressing ψ^t as a combination of two potentials weighted by ξ

$$\psi^{t}(\varepsilon_{e}^{t}) = \xi\psi_{c}^{t}(\varepsilon_{e}^{t}) + (1-\xi)\psi_{t}^{t}(\varepsilon_{e}^{t}), \quad 0 \le \xi \le 1. \tag{11}$$

Here functions ψ_c^t and ψ_t^t are calibrated to the uniaxial compressive and tensile stress-transformation strain responses, and ε_e^t is the equivalent transformation strain defined in Eq. (A1). The resultant back stress-transformation strain responses appear in Fig. 5(a) and the complete fits of the two hystereses in Fig. 5(b). The compressive response captures the hardening behavior of the experimental one, while the unstable behavior exhibited in tension, is modeled using an up-down-up response as shown in the two figures–in the spirit of Ericksen (1975). Details about the calibration of the model are given in Appendix A where the treatment of plastic deformations is included.

4. Numerical results

4.1. Simulation of the bending experiment on NiTi tube with $D/t \approx 18.7$

We first simulate the bending experiment described in Section 2 using the geometric parameters in Table 1 and the constitutive model calibrated in Appendix A. Fig. 6(a) plots the calculated moment-end rotation ($M/M_o - \theta_L/L\kappa_o$) response in which an imperfection with an amplitude of $a = 0.02R$ and $\beta = 100$ was introduced. Included is the response measured in the experiment. Fig. 7 shows a set of corresponding deformed configurations of the domain analyzed with color contours of axial strain superimposed. The calculated response follows the experimental one quite well: the slope of the initial stiff response when the material is in the austenitic phase is reproduced; the moment knee caused by the onset of phase transformation is captured, and so is the level of the subsequent moment plateau during which localized deformation patterns develop. Furthermore the downturn in the response associated with the collapse of the structure is also quite close to that of the experiment.

Bending tends to ovalize tubes, a geometric nonlinearity that reduces their bending rigidity and can precipitate additional instabilities that lead to collapse (Brazier, 1927; Kyriakides and Ju, 1992; Ju and Kyriakides, 1992). To help examine the interaction of ovalization with the induced localized deformation, Fig. 6(b) plots the change in diameter in the plane of bending at the mid-span – site a, and at three other sites, b, c, and d, located at the distances from mid-span indicated in the inset.

Station ① in Fig. 6(a), at a curvature of $1.451\kappa_o$ is close to the end of the initial stiff part of the response before phase transformation commences. Consequently, in configuration ① in Fig. 7, the tube is uniformly bent and is free of any localized deformation. Accordingly, the change in diameter at the four sites is essentially the same indicating uniform ovalization along the length. This station corresponds also to the nucleation of transformation at the thickness depression at b, which is registered by a small drop in moment in Fig. 6(a). The nucleation causes the ΔD at the four sites to start growing at different rates with those at a and b growing at faster rates than at the other two locations. The transformation is in the form of a pair of higher strain inclined bands that are visible in image ② in Fig. 7 at an end-rotation of $1.649L\kappa_o$. The bands have strains of the order of 6% and affect the full wall thickness. At this time a second pair of bands have nucleated at site c located about $3.2D$ from the plane of symmetry. This nucleation is also accompanied by a small drop in the moment. The new bands are visible in image ③ at an end-rotation of $1.772L\kappa_o$ which corresponds to the

nucleation of a third X-shaped pattern at site d, 0.8D from the end of the tube on the right. The third nucleation is also registered by a small drop in the moment. The three pairs of bands are portrayed in image ④ at 1.890$L\kappa_o$. By this time the change in diameter at a has increased to 1.45% and at b to 1.13% while at the other two sites remains below 1%.

The compressive strain in the neighborhood of the plane of symmetry has now reached high enough levels to excite the imperfection, which in turn accelerates further local transformation. This is reflected by the upward trend in the ovality immediately beyond station ④. This has a modest influence on the ΔD at b but none at c and d. At an end-rotation of 2.0$L\kappa_o$, new bands start to nucleate at b oriented towards the mid-span. This results in a very significant increase in the rate of growth of ovality at a and a more modest rate increase at b. The new bands are evident in image ⑤ at 2.168$L\kappa_o$where the bands at c and d are seen to remain unchanged. The ovality at the plane of symmetry is now nearly 3.5%, at b it is 1.6%, and at the other two sites remains below 1%. Nucleation of higher strain bands at b continues as they get organized into a full diamond pattern that can be seen in image ⑥ at $\theta_L = 2.610L\kappa_o$. Simultaneously, transverse bands of higher strain appear on the compressed side, one just opposite the diamond vertex and a second at mid-span. These are transverse wrinkles precipitated by the high ovality and compressive strain in this neighborhood. The wrinkles are a prelude to the onset of collapse that takes place beyond this station indicated by the sharp drop in the moment and the high rate of growth in the local ΔD. In image ⑦ the tube is in a more advanced state of collapse, the moment is on a sharp downward path, and the calculation is terminated. As is the case in other instabilities of inelastic structures, collapse is sensitive to the amplitude of the imperfection adopted in such buckling calculations. For the 2% amplitude adopted here the sharp downturn is very close to that of the experiment. The expanded view of the collapsed zone in Fig. 8 shows the tube to have developed a buckle due to excessive diffuse ovalization affecting a length of about of 2–3 tube diameters––taking the symmetry into account, which is very similar to the buckle in the experiments. The high strain levels incurred by the most ovalized section confirm that parts of it have been plastically deformed.

4.2. Bending of geometrically perfect case

The interaction between ovalization and transformation-induced localized deformation is further illustrated in a bending simulation of the same tube in which no geometric imperfection was introduced. In the absence of an imperfection the moment response, shown in Fig. 9(a), extends to the significantly larger

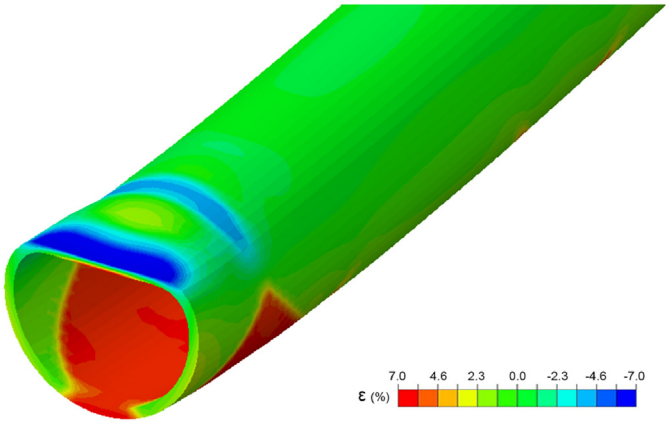

Fig. 8. Expanded view of the buckled section at $x = 0$ that exhibits local diffuse ovalization and plastic deformations corresponding to configuration ⑦ in Fig. 7.

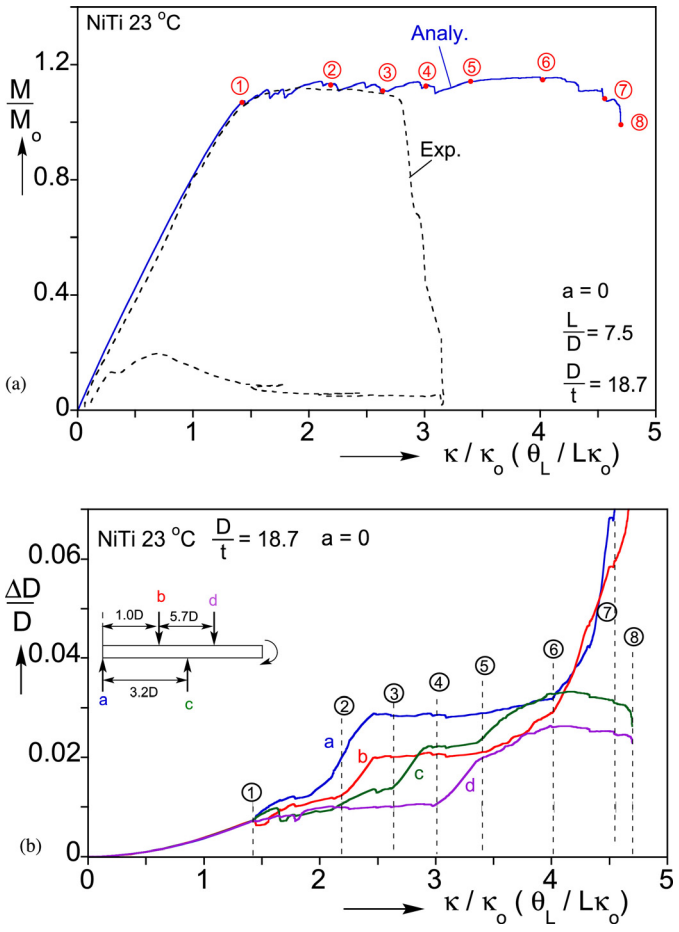

Fig. 9. (a) Calculated moment-end rotation response for tube with $D/t = 18.7$ in the absence of a geometric imperfection. (b) Induced change in diameter in the plane of bending at four sites identified in configuration ② in Fig. 10.

end-rotation of $\theta_L = 4.56L\kappa_o$. This in turn accommodates a more extensive propagation of localization patterns along the length before the tube collapses (see deformed configurations in Fig. 10). Interestingly, X-shaped bands of higher strain nucleate at the same locations as in the imperfect tube in Section 4.1. Hence the change in diameter is monitored at the same four sections labeled in configuration ② as a, b, c, and d. The values of $\Delta D/D$ recorded during the bending history are plotted against the end-rotation in Fig. 9(b).

Nucleation of higher strain bands initiates at a curvature of 1.421$L\kappa_o$ at station ①. Up to this point, the tube bends and ovalizes uniformly. As the curvature increases, transformation in the form of X-shaped pairs of higher strain nucleates first from the thickness depression at b, and then progressively at sites c and d. Each nucleation again registers as a small drop in moment while the ΔD values at the four sites start to deviate from each other. The three pairs of bands are depicted in image ② at $\theta_L/L\kappa_o = 2.188$. By this time additional bands have nucleated at site b causing an upswing in the recorded ΔD at a and b in Fig. 9(b). The growth of ovality at a and b continues due to nucleation of additional bands at site b. The ovality stops growing at these two locations at about 2.48$L\kappa_o$, when local banding forms a complete diamond pattern that is evident in image ③. As this localized deformation was taking place at b, the ovality at site d remained unchanged while that at site c grew modestly.

Local band nucleation has now moved to site c causing an upturn in the local ovality while ΔD at the other three sites remains unchanged. This continues until a second diamond has

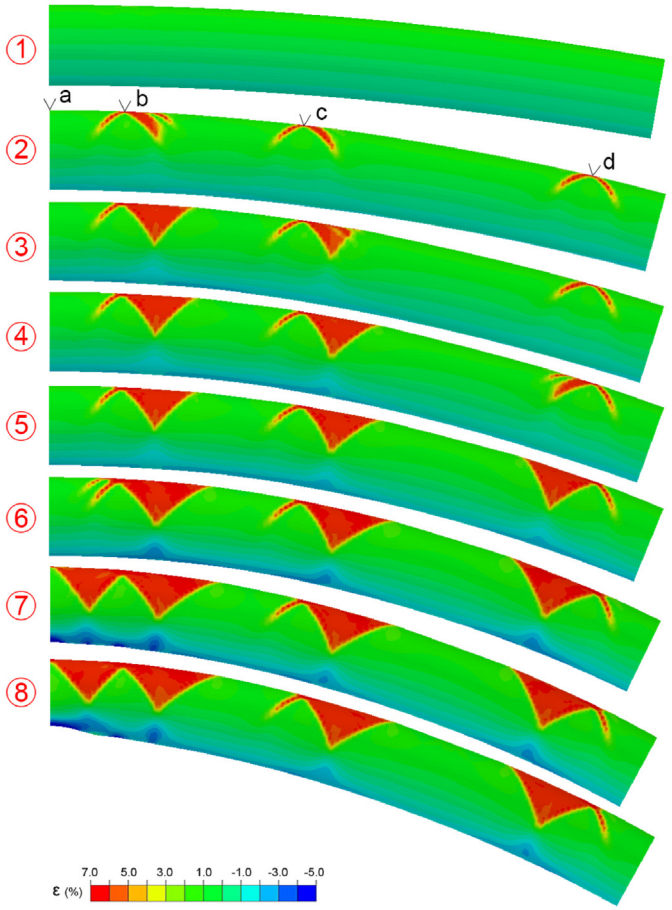

Fig. 10. Sequence of deformed configurations with axial strain contours superimposed corresponding to the numbered bullets on the calculated response in Fig. 9 (a).

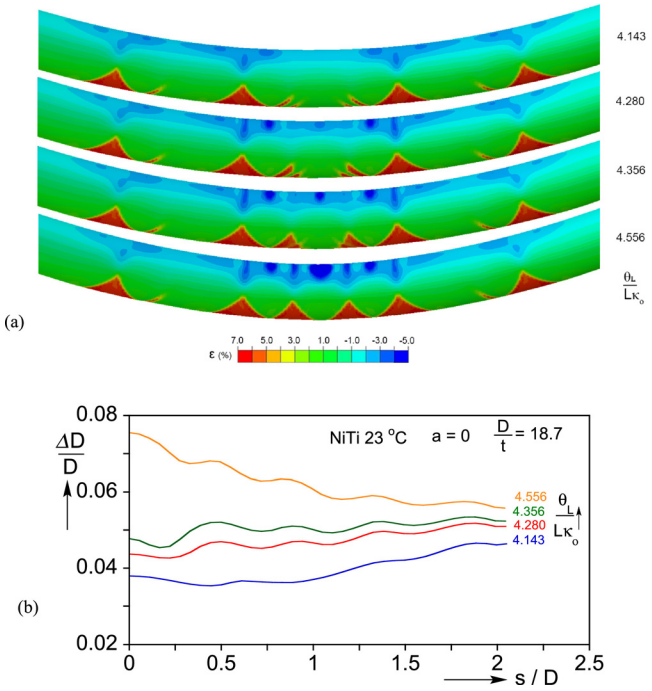

Fig. 11. (a) Deformed configurations of the central section of the tube corresponding to end rotations between stations ⑤ and ⑥ in Fig. 9(a) (images reflected for better visualization). The superimposed axial strain contours show gradual evolution of transverse wrinkles on compressed side. (b) Axial profiles of ΔD that also illustrate the evolution of wrinkling close to the symmetry plane at $x = 0$.

filled in at site c that can be seen in image ④ at $\theta_L = 3.010L\kappa_o$. With the formation of the second diamond, nucleation of bands moves to site d as is evident from image ④. The local ΔD starts increasing, while the values recorded at the other three sites remain relatively unchanged. The nucleation of bands at site d continues until about $3.397L\kappa_o$ when they have evolved into a third full diamond observed in image ⑤. As the end rotation increases further, the diamonds at c and d fill in concurrently causing the simultaneous gradual increase in ovality at b, c, and d observed between station ⑤ and ⑥ in Fig. 8(b). At an end-rotation of $4.021L\kappa_o$ that corresponds to image ⑥ new bands are seen to be nucleating on the left of the diamond at site b, while the diamonds at c and d are more expanded.

The new banding results in a sharp increase in the ΔD at both the plane of symmetry and site b and a gradual downturn in the moment. The structure is quickly losing local stiffness and is beginning to collapse. By station ⑦ at $\theta_L = 4.556L\kappa_o$, a new high strain diamond has formed next to the plane of symmetry, the ovality at both of these sites has climbed to above 6%, and the moment has dropped significantly. Simultaneously the diamonds at sites c and d appear unchanged, while the local ΔD starts to decrease due to unloading. In image ⑧ a local buckle has formed at mid-span similar to the one in Fig. 8. Clearly, the nucleation of high strain bands on the tensioned side of the bent tube that evolve into diamond patterns induces the local increase in ovalization with a consequent local reduction in bending rigidity.

A short video–M-k-DD_187-0.mov–that combines the moment-end rotation response, the change in diameter at points a and d with the corresponding tube configurations is provided for further clarity under supplementary material.

Another consequence of the diamond formation is illustrated in Fig. 11(a), which shows four configurations of the central section of the tube–mirrored about the plane of symmetry–between stations ⑤ and ⑥. At $\theta_L/L\kappa_o$ of 4.143, it is evident that opposite to each diamond on the compressed side a concentration of compressive strain forms. At the slightly higher end-rotation of $4.280L\kappa_o$, four crosswise strain concentrations appear opposite the inner diamonds and one at mid-span. At $4.356L\kappa_o$ the two central diamonds are partially developed and the five compressive strain concentrations strengthen. At an end-rotation of $4.556L\kappa_o$ that corresponds

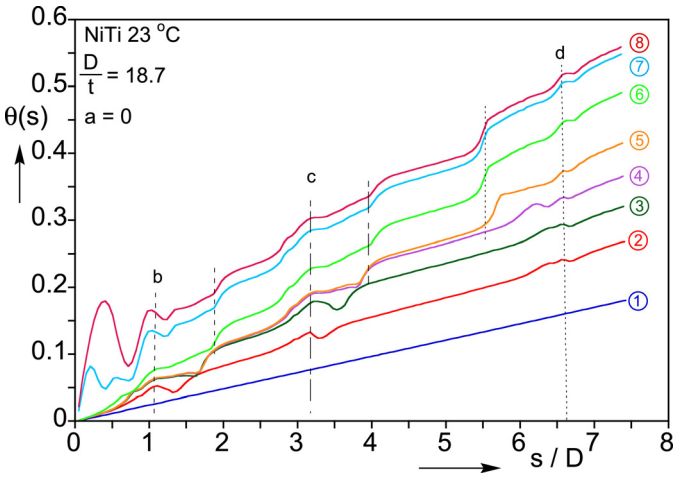

Fig. 12. Average slope along the length of the tube corresponding to the configurations in Fig. 10 displaying local undulations caused by the formation of diamond patterns.

to station ⑦, the central diamonds are now fully developed and this has added two more compressive strain concentrations. The compressive strain levels in these zones are high enough to lead to local wrinkling. The wrinkles are depicted in Fig. 11(b) that shows profiles of ΔD over the central span of the tube. The wrinkles are fully developed by $\theta_L/L\kappa_o = 4.280$. Their amplitudes grow with end-rotation with the central wrinkle localizing and leading to local collapse. It is worth mentioning that similar wrinkling patterns induced by diamond-like patterns of Lüders banding were reported in Hallai and Kyriakides (2011b).

The effect of the localized deformation on the overall configuration of the structure is demonstrated in Fig. 12, which plots the local slope, $\theta(s)$, along the length of the tube corresponding to the eight stations on the response ($\theta(s)$ is the average of the slopes of the most tensioned and compressed generators). At station ①, before the onset of transformation, the $\theta - s$ profile is linear implying that the tube is bent to a uniform curvature. Profile ② has a higher average slope but the nucleation of X-shaped bands of higher strain caused local slope undulations at sites b, c, and d. Interestingly, these undulations remain as the tube is bent to higher curvature. In profile ③ at an end-rotation of $2.637L\kappa_o$, the average slope has increased accordingly. However, the bands that emanate from the thickness depression at b and propagate toward the right have resulted in some local flattening of the top, that appears as a local reduction in slope. The extent of this change in slope corresponds approximately to the base of the diamond and is bounded by the two dashed lines drawn in the figure. This disturbance remains in profile ④ at an end-rotation of $3.010L\kappa_o$, where a second similar local reduction in slope developed at c due to the appearance of the second diamond to the right of this point. In profile ⑤ at $3.397L\kappa_o$, a local increase in slope takes place on the left of site d due to the nucleation of the third diamond pattern. Profile ⑥ at $4.021L\kappa_o$ has a corresponding increase in average slope, however, the local changes in slope introduced by the previous nucleations of diamonds are maintained. In profiles ⑦ and ⑧ banding has moved close to the plane of symmetry causing significant changes in slope as the tube buckles locally. The variations in slope indicate that the localized deformation and ovalization affect the local curvature of the tube as well.

In summary, the local nucleation of higher deformation bands and diamond patterns result in local changes in the curvature of the tube. Similar configurational effects were observed in the much thicker tube –$D/t \approx 8.5$– analyzed in Jiang et al. (2017b). However, in that case the diamond patterns propagated sequentially from the plane of symmetry to the other end. Consequently, the tube developed two curvature regimes such as those observed in the corresponding experiment in Bechle and Kyriakides (2014).

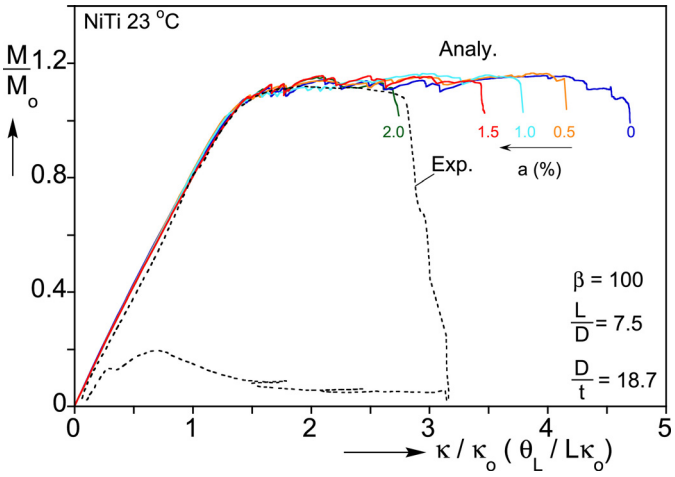

Fig. 13. Calculated moment-end rotation responses for different values of imperfection amplitude for the $D/t = 18.7$ tube.

4.3. Effect of imperfection amplitude

In the analysis of inelastic buckling of shell structures instability is usually primed by the introduction of a small geometric imperfection to the model tube. The results in Figs. 9–12 demonstrate that in the case of the $D/t \approx 18.7$ tube analyzed the localized deformation induced by phase transformation perturbs the structure sufficiently to cause it to buckle in the absence of a geometric imperfection. However, the stability of the structure remains sensitive to inherent stimuli and this sensitivity is demonstrated in Fig. 13, where the amplitude of the axisymmetric imperfection in Eq. (2), a, is varied. An amplitude of $0.005R$ reduces the end rotation by about 13%, for $0.01R$ by 20%, for $0.015R$ by 26%, and for $0.02R$ by 42%. It is worth pointing out that similar sensitivity of collapse to this type of imperfection was reported in Hallai and Kyriakides (2011b) for bending of steel tubes with Lüders bands. By comparison, the experimental response included in Fig. 13 collapses at an end rotation of $2.82\kappa_o$, which is close to that of the largest imperfection considered of $a = 0.02R$. In physical experiments the structure is perturbed by stress concentrations at the boundaries, by geometric imperfections, and by material properties variations. Thus, this collapse curvature is influenced by all such perturbations.

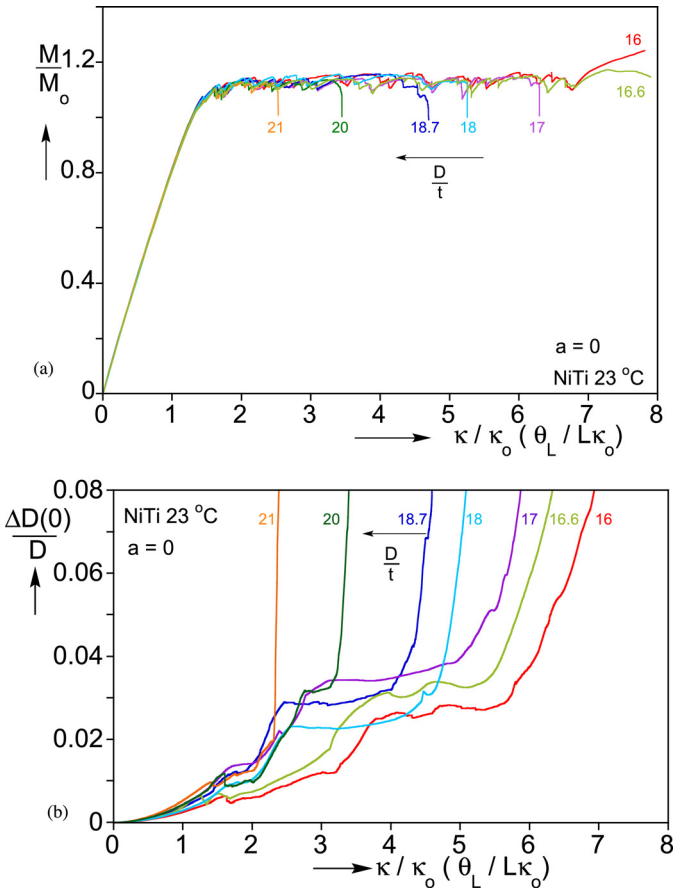

Fig. 14. (a) Calculated moment-end rotation responses of tubes with D/t ratios ranging from 16 to 21. (b) Change in diameter at the location of the buckle plotted against the end rotation.

5. Parametric study

5.1. Effect of Tube D/t

As in hardening metal alloy tubes, the response and stability of NiTi tubes under bending is strongly influenced by D/t (Kyriakides and Ju, 1992; Ju and Kyriakides, 1992). This effect is demonstrated in Fig. 14(a), which plots the calculated moment-end rotation response of tubes with D/ts ranging from 16 to 21. The outer diameter of all cases is the same as that in Table 1 but the wall thickness is varied. Thickness depressions are introduced to all tubes at a distance D from $x = 0$. All cases exhibit an initial stiff bending rigidity, which decreases as D/t increases. However, the normalizations of the moment and curvature adopted results in the coalescence of the different responses. The decrease in bend-

Table 2
End-rotations at buckling of different D/t tubes.

D/t	21	20	18.7	18	17	16.6	16
$\theta_{Lc}/L\kappa_o$	2.534	3.542	4.709	5.248	6.268	7.363*	8.142*

* correspond to the local moment maximum.

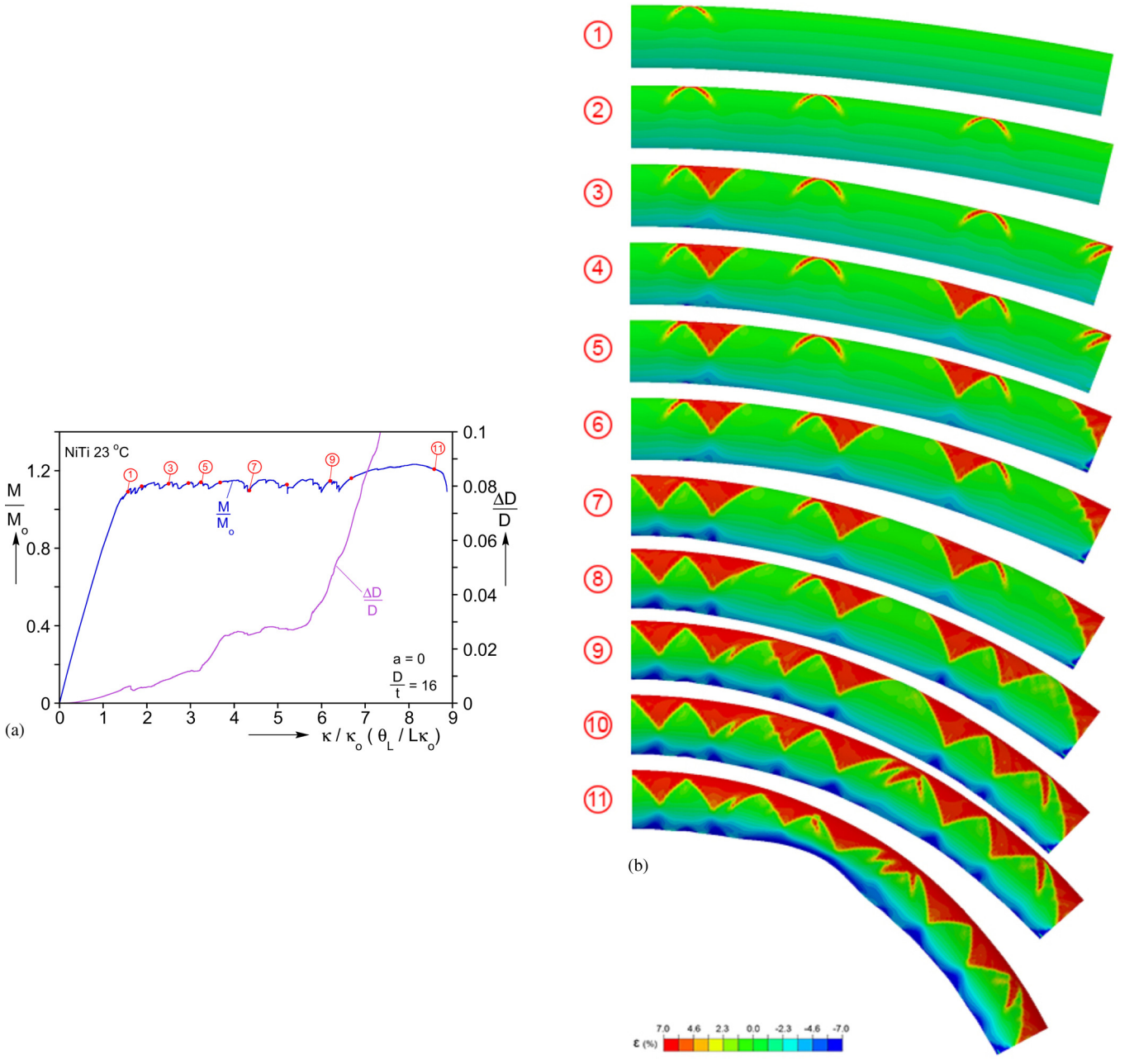

Fig. 15. (a) Moment-end rotation and corresponding change in diameter for a tube with $D/t = 16$ for which transformation is completed and tube buckles during stable material behavior. (b) Corresponding deformed configurations that show tensioned side covered with diamond patterns.

ing rigidity is accompanied by an increase in the induced ovality evident in Fig. 14(b), where the change in diameter at the symmetry plane is plotted against the end rotation. The elastic behavior is terminated by the onset of transformation represented by the distinct knee in the responses. For all D/ts, high strain first nucleated at the thickness depression on the tensioned side in the form of two narrow bands along the two characteristics. All cases exhibited additional nucleation sites rather randomly located, which subsequently evolved into diamonds. During the evolution of transformation the moments trace rugged plateaus, which because of the normalization share the same level (Fig. 14(a). The number of high strain diamond patterns that form and the extents of the moment plateaus vary with D/t as transformation is interrupted by buckling. The pauses in the growth of $\Delta D(0)$ observed in most of the profiles in Fig. 14(b) are associated with the nucleation and spreading of diamond patterns at sites that are away from the $x = 0$ where the ΔD is recorded. Going from D/t of 21 to 17 the tubes buckled at progressively larger end rotations (see Table 2) leaving part of the tube untransformed and the moment plateau incomplete. Buckling manifests as local diffuse ovalization at the mid-span similar to that shown in Fig. 7. It is also accompanied by the sharp drop in moment observed in Fig. 14(a) and the significant upturn in the local $\Delta D/D$ seen in Fig. 14(b).

For the tubes with D/t of 16.6 and 16, high strain diamond patterns covered the whole tensioned side of the tube and the moment plateau was completed. This behavior is demonstrated in the moment- and ΔD-end rotation results and by the deformed configurations Fig. 15 for $D/t = 16$. With the completion of transformation the material follows the stiff response of martensite illustrated in Fig. A1. Consequently, the moment starts to harden again and the deformation along the length of the tube becomes uniform. It is important to point out that, since the transformation strain in compression is smaller than in tension, the compressed side enters the martensitic phase earlier. The transformation stress is also higher, so as the curvature increases the compressed side yields causing a gradual reduction in the bending rigidity eventually leading to a moment maximum for both D/ts. Beyond the maximum, ovalization localizes at a location $3.5D$ from the plane of symmetry – see image ⑪ in Fig. 15(b). As is customary, the curvature at the moment maximum is taken as the collapse curvature for these two D/ts.

Summarizing, under bending higher D/t tubes buckle and collapse before transformation affects the entire structure. Collapse leads to plastic deformations and potentially to rupture, violating the recoverable nature of pseudoelastic SMAs. Intermediate D/t tubes can complete the transformation to martensite, but further bending is limited once again by plastic deformations and potentially failure.

5.2. Mesh sensitivity of the solution

The mesh adopted for most of the calculations reported here involves nearly cubical elements with two through the wall thickness for a total of 650,000 degrees of freedom. It was chosen after confirming that it is dense enough to capture the finer features of the localized deformation patterns observed in the bending experiments. As in the bending results of Jiang et al. (2017b), the softening branches of the tensile stress-strain response result in a mild mesh-sensitivity of the solution (Needleman, 1988). To quantify this effect, the bending of the base case of $D/t = 18.7$ was repeated using two additional mesh densities having 3 and 4 elements through the thickness, for an imperfection amplitude of $a = 0.02R$. This results in 100 and 130 elements around the half circumference and a total of 2.17×10^6 and 4.59×10^6 degrees of freedom respectively. The solutions trace nearly identical moment-end-rotation responses with some minor differences in the moment

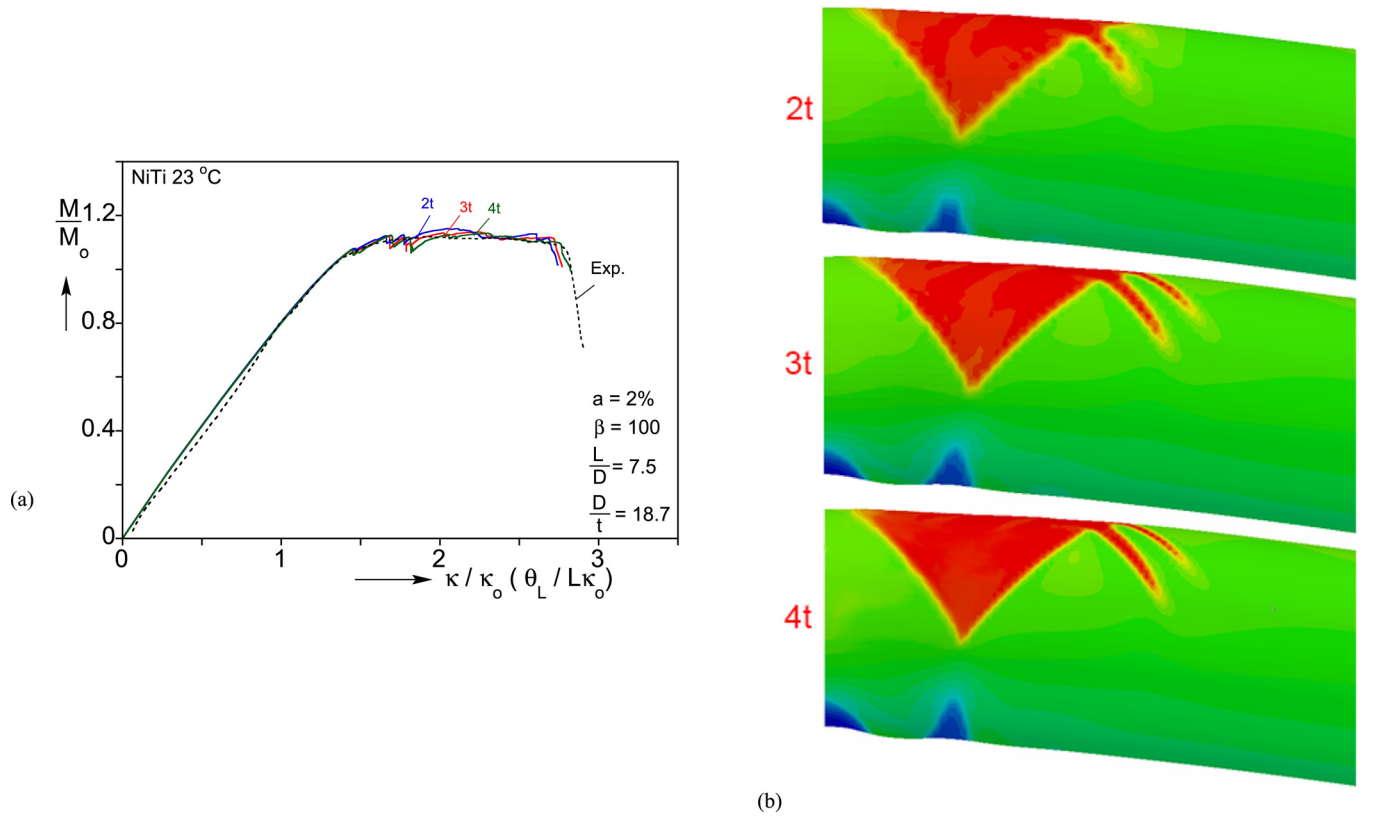

Fig. 16. Mesh sensitivity study. (a) Moment-end rotation responses for three mesh densities. (b) Expanded views of diamond pattern near the symmetry plane at $x = 0$ calculated for the three meshes.

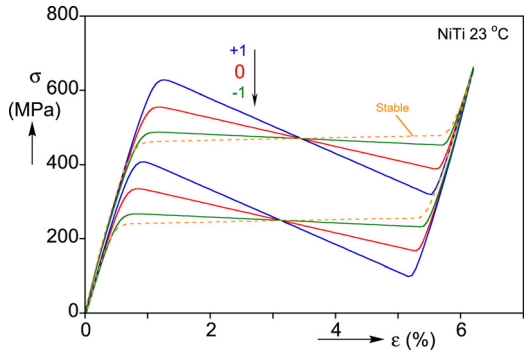

Fig. 17. Tensile stress-strain response with different softening slope considered– "0" corresponds to the one adopted in most of the calculations.

undulations (see comparison in Fig. 16(a). Deformation localizes in a very similar manner developing one main diamond pattern near the mid-span that excites the axisymmetric imperfection, and causes buckling and collapse as described in Section 4.1. This section of the domain of each of the three meshes is shown expanded in Fig. 16(b). As was the case for the results of the $D/t \approx 8.5$ in Jiang et al. (2017b), the three diamond pattern are alike but refining the mesh narrows the transition zone between the high strain domain and the adjoining untransformed domain. This affects most prominently the protruding bands and the edges of the diamond. Remedies for these minor mesh sensitivity effects were discussed in Section 5.1 of Jiang et al. (2017b) and will not be repeated here.

5.3. Effect of the softening modulus

The slope of the softening branches introduced to the tensile material response in Fig. 5(b), is approximately the one measured in the sandwich tension test reported in Hallai and Kyriakides (2013) (used also in Jiang et al., 2017a,b). To examine the effect of this slope on the bending response of our $D/t = 18.7$ tube, the numerical simulations are repeated for the two tensile responses shown in Fig. 17 together with the one used thus far, identified as "0". No axisymmetric imperfection is introduced in order to allow the development of more diamond patterns in the domain. The case designated as "+1" has nearly double the negative slope of the base case, and for the one identified by "-1" the slope is approximately half that of "0". The moment-end-rotation responses are individually compared to that calculated for the base material in Figs. 18(a) and 19(a) respectively. In both cases high strain bands nucleate first from the thickness depression on the tensioned side, trace moment plateaus during which bands nucleate at additional sites, and progressively get organized into diamond shaped patterns. The moment plateaus are at similar levels, have similar extents to that of the "0" material, and each terminates when the tube buckles and collapses at the symmetry plane. Sets of corresponding deformed configurations appear in Figs. 18(b) and 19(b). Other than the first nucleation from the thickness depression, the number and locations of nucleation sites are different for the three materials. Material "−1" has four nucleation sites, while "0" and "+1" each have 3 but at different locations.

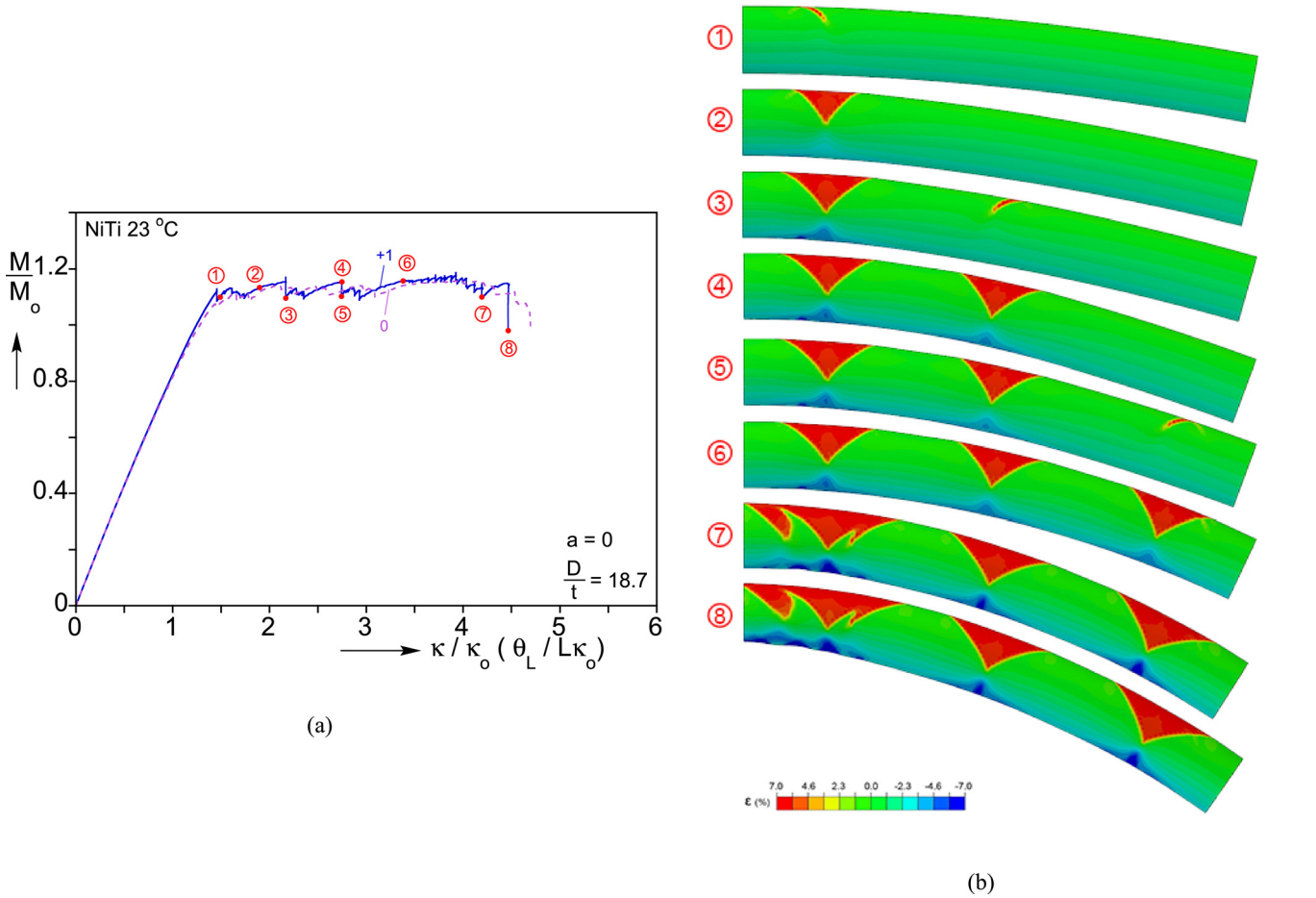

Fig. 18. (a) Moment-end rotation response and (b) corresponding deformed configurations for material "+1" ($D/t = 18.7$).

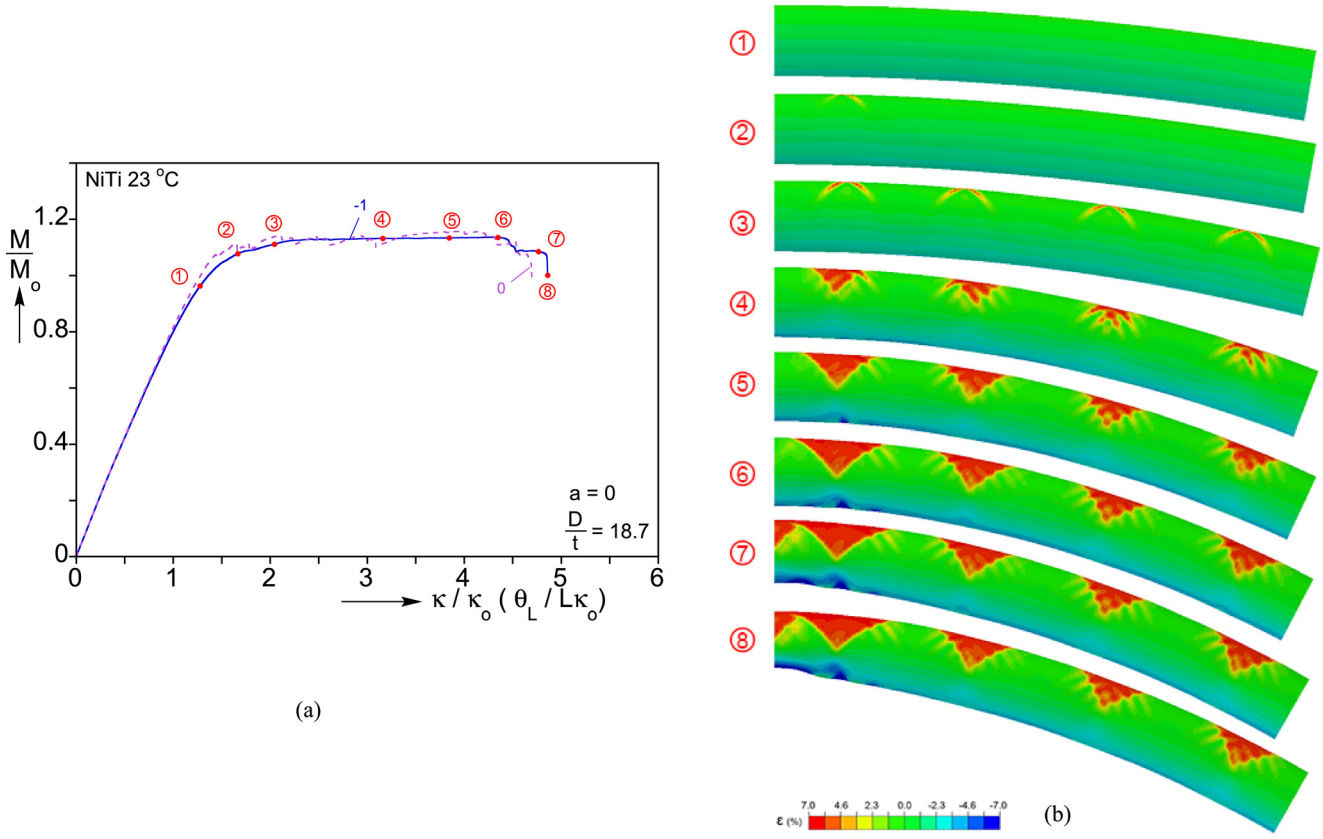

Fig. 19. (a) Moment-end rotation response and (b) corresponding deformed configurations for material "−1" (D/t = 18.7).

Four diamond-like deformation patterns develop almost simultaneously for "−1." They are not accompanied by any significant drop in the moment and, as a result, the moment-end rotation response for this material is much smoother than those of the other two cases. The diamond close to the symmetry plane is almost complete with nearly smooth edges, while the other three have shorter bases, are incomplete, and weaker with uneven edges. As mentioned in our previous works in which partially unstable material responses are used (e.g., Aguirre et al., 2004; Hallai and Kyriakides, 2011b), there is a lower limit in the negative slope required for localization and propagation of higher deformation patterns to develop. The slope of "−1" appears to be close to that limit. By contrast, for "+1" the nucleations result in sharp drops in moment making the moment-rotation response in Fig. 18(a) much more rugged than that of the base material. Diamonds develop sequentially, and when fully developed have a wider base, and sharper boundaries. Clearly, the stronger softening makes the localization and propagation of higher strain more pronounced.

In summary, the value of the softening slope can be viewed as the strength of the material instability. It must exceed a minimum value for nucleation and propagation of higher strain to develop. More negative slopes produce more distinct localization patterns but otherwise their effect on the localization events and on the stability of the structures appears to be limited. Measurement of the softening slopes during both loading and unloading would be of great help to such models.

For completeness, a material with a mildly positive slope in tension that maintains the tension/compression asymmetry is also considered – drawn with a dash line in Fig. 17. Its effect on the moment-curvature response and on the deformation of the structure is summarized in Appendix B.

5.4. Symmetric material model

The localized deformation exhibited by pseudoelastic NiTi under primarily tensile loads is macroscopically similar to Lüders banding in low carbon steel (e.g., Kyriakides and Miller, 2000). A distinct difference is that in such steels the dislocation driven localized banding occurs under both tensile and compressive loadings. Furthermore, typical Lüders strain values range between 1% and 3%. In their study of the effect of Lüders banding on the response and stability of steel tubes under bending, (Hallai and Kyriakides, 2011a,b) showed that the induced localized deformation and the associated local acceleration in the growth of ovalization tend to affect significantly the stability of the structure leading to premature buckling and collapse (see also Aguirre et al., 2004). Motivated by this sensitivity the effect of symmetric softening on the bending response of the D/t = 18.7 tube is also evaluated. Thus, the material model is assigned the tensile softening behavior shown in Fig. 5(b) to compression as well. The same small thickness depression used in previous simulations is introduced to the model but no axisymmetric imperfection.

The resultant moment- and change in diameter-end rotation at the symmetry plane responses are plotted in Fig. 20(a). Included for comparison are the corresponding responses of the asymmetric material model–case "0". Fig. 20(b) shows a set of corresponding deformed configurations. Localized banding initiates first from the thickness depression on the tensioned side leading to a lower

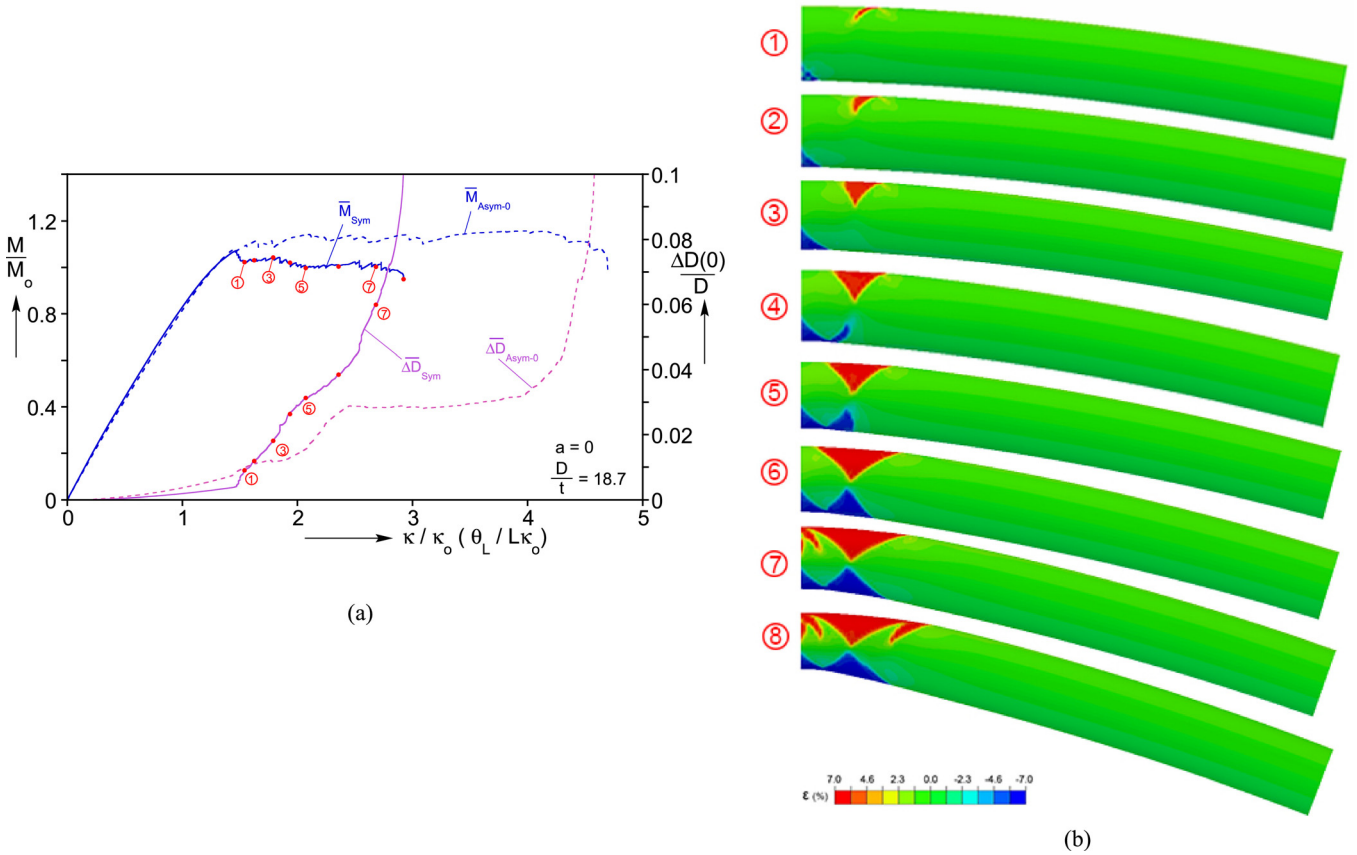

Fig. 20. (a) Moment-end rotation response and corresponding change in diameter for a material that is unstable both in tension and compression ($D/t = 18.7$). (b) Corresponding deformed configurations.

moment than that of the asymmetric material model. This leads to the first moment drop in the response, and a corresponding upswing in ΔD. Shortly thereafter, a compressive high strain (half) diamond nucleates on the compressed side at the symmetry plane that can be seen in image ①. In image ② the tensile and compressive domains are seen to have grown, while in image ③ the banding on the tensile side has evolved into a small diamond. The local higher deformation in turn accelerates the growth of ovalization at the symmetry plane. In image ④ the base of the tensile diamond has widened, while new bands emanating from the existing diamond on the compressed side have appeared. In image ⑤ the tensile diamond has widened further and a diamond is developing opposite to it on the compressed side that is seen completely formed in image ⑥. In image ⑦ the diamonds are fully developed on both sides, and new bands emanate from the edges of the tensile diamond. This leads to additional increase in the local ovality, further destabilization, and buckling by diffuse local ovalization that can be seen in image ⑧. The symmetric formation of tensile and compressive diamonds replicates the symmetric arrangement of diamond patterns induced by Lüders banding observed in the Hallai and Kyriakides works. However, here the strain is significantly larger and the diamonds are fuller with more distinct boundaries. The larger strain causes larger ovalization, which in turn reduces the local bending rigidity of the structure and leading to an earlier collapse. Comparing the behavior of the symmetric and asymmetric material, the moment plateau is lower on average by about 12% due to the absence of the stiffening effect of the hardening in compression. Furthermore, the asymmetric material allowed the nucleation of several more tensile diamonds, which is responsible for the extended plateau in the $\Delta D - \theta_L$ trajectory in Fig. 20(a). This delayed collapse until a much larger end rotation was reached. By contrast, the symmetric material limited nucleation of diamonds to the neighborhood of the symmetry plane, caused a faster growth of the local ovalization, which destabilized the structure at a much lower end rotation.

6. Summary and conclusions

Pseudoelastic NiTi tubes and rods exhibit tension/compression asymmetry. Under tension, transformation induces strains of nearly 7% that localizes and spreads under nearly constant stress. Under compression, the transformation stress is nearly double, the strain is approximately one-half, grows homogeneously and exhibits hardening behavior. In pure bending experiments on relatively low D/t tubes this asymmetry results in zones of localized curvature with diamond-shaped higher strain patterns of martensite developing on the tensioned side, and smaller more uniform strain in compression. The higher curvature and diamond patterns tend to spread to the rest of the structure with the moment remaining nearly constant. Experiments on higher D/t tubes exhibit very similar localized deformation in the form of diamond patterns, which, however, now interact more strongly with bending induced ovalization of the cross section. This interaction can in turn cause local buckling and collapse of the structure.

The phenomenological constitutive model of the complex asymmetric behavior of pseudoelastic NiTi in Jiang et al. (2016b, 2017b), suitably tailored to the present material and problem, has been used in finite element analysis of the bending response and stability of higher D/t NiTi tubes. Simulation of a bending experiment on a $D/t = 18.7$ tube demonstrated that the higher strain diamond patterns of martensite that develop on the tensioned side cause a local increase in ovality of the cross section that

degrades the local bending rigidity of the structure. In the presence of small geometric imperfections, and other stress risers, this degradation evolves into a buckle in the form of diffuse local ovalization that precipitates collapse.

The model was used to perform a parametric study of the response and stability of NiTi tubes with the intermediate range of D/ts of 16 to 21. The main findings of this study can be summarized as follow:

- The stability of the tubes is strongly dependent on D/t. For higher D/ts the interaction of ovalization and local transformation is more pronounced. Transformation and the associated diamond patterns affect an increasingly shorter length of tube causing local buckling at smaller end-rotations. For lower D/ts in this range, transformation and diamond patterns spread over the whole length of the tube. When the transformation spreads over the whole length, the tube starts deforming uniformly with increasing moment. Eventually, the material plasticizes and the structure develops a moment maximum beyond which it collapses.
- The stability of the tubes is very sensitive to geometric imperfections, particularly ones that tend to excite axial wrinkling. This sensitivity is similar to that exhibited by metal tubes with hardening elastic-plastic behavior but for NiTi the effect of imperfections can be accentuated by localized transformation induced strain.
- The present constitutive model is rate independent and, as result, the softening modulus of the tensile response can cause some sensitivity to the mesh. By considering increasingly more refined meshes it was demonstrated that the mesh does not influence the overall structural response or its stability. Its main effect is limited to the transition zone separating transformed and untransformed zones, an observation that is in concert with the results of Jiang et al. (2017b).
- The strength of the material instability, governed by the slope of the softening branch of the tensile response, has only minor influence on the moment-end rotation response and on the stability of the tube. However, the slope must be "negative enough," which presently is decided by repeated trials. This points to the dire need for experimental methods for measuring the unstable branch of the material response (e.g., Hallai and Kyriakides, 2013).
- The hardening nature of the compressive response of these tubes has a stabilizing effect on the structure. A symmetric material model based on the tensile softening response results in diamond patterns on the compressed side and makes the structure much more prone to buckling.

Declaration of Competing Interest

All authors declare that they have no known competing financial interests or personal relationships that could have appeared to influence the work reported in this paper.

Acknowledgments

The authors acknowledge with thanks the financial support received for this work from the National Science Foundation under grant no. CMMI-1762389.

Supplementary materials

Supplementary material associated with this article can be found, in the online version, at doi:10.1016/j.ijsolstr.2019.12.017.

Appendix A: Constitutive model calibration

The equivalent transformation strain, ε_e^t, in (11) is related to the strain invariants as follows

$$\varepsilon_e^t = J_2' f(J_r),\quad J_r = J_3'/J_2', \tag{A.1a}$$

where

$$J_2' = \left(2e_{ij}^t e_{ij}^t/3\right)^{1/2},\ J_3' = \left(4e_{ij}^t e_{jk}^t e_{ki}^t/3\right)^{1/3},\ e_{ij}^t = \varepsilon_{ij}^t - \varepsilon_{kk}^t\delta_{ij}/3. \tag{A.1b}$$

The scaling function takes the form

$$f(J_r) = \cos\left\{\cos^{-1}\left[1 - a\left(J_r^3 + 1\right)\right]/3\right\},\ -1 \le f \le 1 \tag{A.1c}$$

(see also Sedlak et al., 2012) and a is a parameter governing the asymmetry. The weight function $\xi(J_r)$ facilitates the generalization of Eq. (11) to general strain states. The function

$$\xi(J_r) = \frac{f(J_r) - f(1)}{f(-1) - f(1)} \tag{A.2}$$

satisfies the finite moduli constraints at the limit $J_r = 0$ discussed in Jiang and Landis (2016). Adopting $f(1) = 0.62$ for extension ($\xi = 0$), and $f(-1) = 1$ for compression ($\xi = 1$), the parameter becomes $a = 0.9533$. The back stress then becomes

$$\sigma_{ij}^B = \xi\frac{d\psi_c^t}{d\varepsilon_e^t}\frac{\partial\varepsilon_e^t}{\partial\varepsilon_{ij}^t} + (1-\xi)\frac{d\psi_t^t}{d\varepsilon_e^t}\frac{\partial\varepsilon_e^t}{\partial\varepsilon_{ij}^t} + \left(\psi_c^t - \psi_t^t\right)\frac{d\xi}{dJ_r}\frac{\partial J_r}{\partial\varepsilon_{ij}^t}. \tag{A.3}$$

Reduction of (A.3) to the uniaxial setting results in

$$\sigma_{11c}^B = \frac{d\psi_c^t}{d\varepsilon_e^t}\frac{\partial\varepsilon_e^t}{\partial\varepsilon_{11}^t}\ \text{ and }\ \sigma_{11t}^B = \frac{d\psi_t^t}{d\varepsilon_e^t}\frac{\partial\varepsilon_e^t}{\partial\varepsilon_{11}^t}. \tag{A.4}$$

Substituting (A.4) into (6) in turn yields the following

$$|\sigma_{11c}| - f(-1)\frac{d\psi_c^t}{d\varepsilon_e^t} = \sigma_{oc}\ \text{ and }\ \sigma_{11t} - f(1)\frac{d\psi_t^t}{d\varepsilon_e^t} = \sigma_{ot}, \tag{A.5}$$

where σ_{oc} and σ_{ot} are respectively the sizes of the compressive and tensile transformation surfaces.

Calibration

The potential ψ_c^t is calibrated by fitting it to the compressive response in Fig. x using the expression

$$\frac{d\psi_c^t}{d\varepsilon_e^t} = h_0\varepsilon^t + (h_1 - h_0)\left(\varepsilon^t - \frac{1-e^{-b\varepsilon^t}}{b}\right) + (h_2 - h_1)\begin{cases} 0 & 0 \le \varepsilon^t \le \varepsilon_1 \\ (\varepsilon_2 - \varepsilon_1)\left(2.5\zeta^4 - 3\zeta^5 + \zeta^6\right) & \varepsilon_1 \le \varepsilon^t \le \varepsilon_2 \\ 0.5(\varepsilon_2 - \varepsilon_1) + (\varepsilon^t - \varepsilon_2) & \varepsilon^t \ge \varepsilon_2 \end{cases}, \tag{A.6}$$

where $\zeta = (\varepsilon^t - \varepsilon_1)/\varepsilon_2 - \varepsilon_1)$ and $\{b,\ h_0, h_1, h_2, \varepsilon_1, \varepsilon_2\}$ take the values listed in Table A1.

The same functional form (A.6) is used to fit the tensile response. Note that the added softening branches replace the upper and lower stress plateaus as shown in Fig. 5. The parameters of this fit are included in Table A1. The difference in size between the compressive and tensile transformation surfaces, σ_{oc} and σ_{ot}, is represented through the strain invariant J'_3 in (A.1) as follows:

$$\sigma_o = \begin{cases} \sigma_{oc} & \eta \le 0 \\ \sigma_{oc} + (\sigma_{ot} - \sigma_{oc})\left(10\eta^3 - 15\eta^4 + 6\eta^5\right) & 0 \le \eta \le 1 \\ \sigma_{ot} & \eta \ge 1 \end{cases}, \tag{A.7}$$

where $\eta = (J'_3 - 0.01)/0.0098$.

Table A1
Model parameters for phase transformation responses.

Parameter	E (GPa)	ν	σ_o (MPa)	b	h_o (GPa)	h_1 (GPa)	h_2 (GPa)	ε_1 (%)	ε_2 (%)
Comp.	66.3	0.425	120.7	2500	1179	2.78	117.9	2.8	3.4
Tens.	66.3	0.425	115.4	2500	1909	−12.54	100.6	2.8	3.4

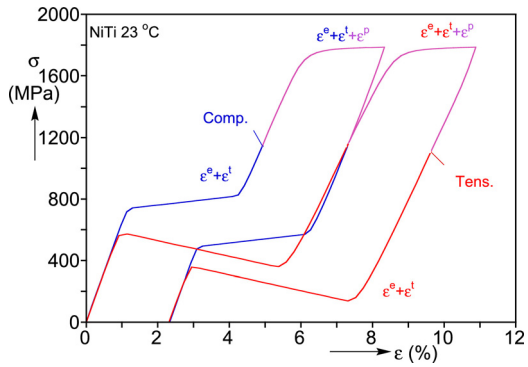

Fig. A1. Tensile and compressive stress-strain responses illustrating the effect of plasticity.

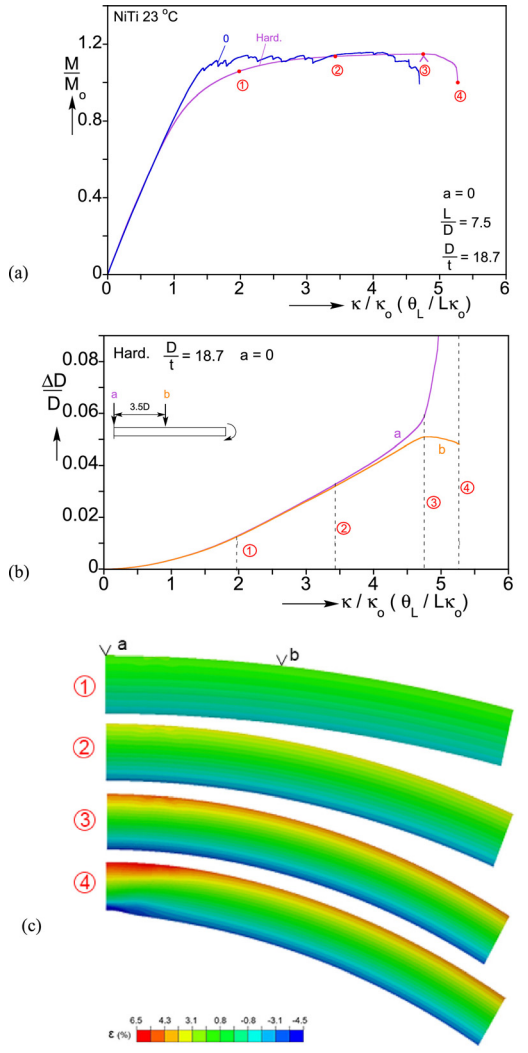

Fig. B1. Results for a material with mildly hardening behavior in tension. (a) Moment-end rotation response; (b) change in diameter at two sites, and (c) four deformed configurations with axial strains superimposed.

For the purposes of the present calculations the material is assumed to yield at the same stress in tension and compression with the following hardening behavior

$$\sigma_y(\varepsilon_e^p) = \sigma_y^0\left[1+\frac{2}{\pi}h^p\tan^{-1}(c\varepsilon_e^p)\right],\quad \varepsilon_e^p = \int_t \dot{\varepsilon}_e^p dt, \tag{A.8}$$

with the three parameters taking the values: $\sigma_y^0 = 1.24$ GPa, c = 1650 and $h^p = 0.446$. Fig. A1 illustrates the effects of plastic deformations in the uniaxial setting.

Appendix B. Bending Response for Asymmetric Stable Material

As a complement to the study of the effect of the slope of the tensile material response of Section 5.3, here we present results in which the tensile response is assigned a small positive slope, while maintaining the monotonic compressive response in Fig. 4. The calculated moment-end-rotation response for the D/t = 18.7 tube is plotted in Fig. B1(a) together with the response of the softening tensile material–case "0". Fig. B1(b) plots the change in diameter $\Delta D/D$ against the end-rotation at two locations: $x = 0$ marked as a, and $x = 3.5D$ marked as b. Fig. B1(c) portrays a select set of configurations with the strain field superimposed. As expected, the moment exhibits nonlinearity earlier but traces a monotonic trajectory until a maximum is achieved at κ/κ_o = 4.762 (marked with "^"). The deformation remains axially uniform until the maximum is approached. The homogeneity is demonstrated from the strain fields in images ①-③ and is also implied by the near coincidence of the $\Delta D - \kappa$ responses in Fig. B1(b) up to just before point ③. The change in diameter grows in the traditional parabolic fashion with curvature reaching a value of about 5% by station ③. This ovality is responsible for the gradual reduction in the bending rigidity leading to the attainment of the load maximum. Beyond this point the deformation localizes in the neighborhood of the mid-span. ΔD at this site starts growing excessively, while away from it the structure unloads because of the decreasing moment. Locally, the transformation has been completed for both tension and compression, so the material is in the stiff martensitic phase. The induced diffuse ovalization leads to the collapse at this site that can be seen in image ④. In other words, stable material behavior in both tension and compression results in a stable deformation of the tube reminiscent of the bending behavior of hardening metal alloy tubes (Kyriakides and Ju, 1992). The growing ovalization eventually results in a limit load and the usual localization and collapse. The curvature at the load maximum is about 18% higher than the corresponding value for the softening material.

References

Abeyaratne, R., Knowles, J.K., 2006. Evolution of Phase Transformations: a Continuum Theory. Cambridge University Press, New York.
Aguirre, F., Kyriakides, S., Yun, H.D., 2004. Bending of steel tubes with Lüders bands. Int. J. Plast. 20, 1199–1225.
Bechle, N.J., Kyriakides, S., 2014. Localization in NiTi tubes under bending. Int. J. Solids Struct. 51, 967–980.
Bechle, N.J., Kyriakides, S., 2016a. Evolution of localization in pseudoelastic NitI tubes under biaxial stress states. Int. J. Plast. 82, 1–31.
Bechle, N.J., Kyriakides, S., 2016b. Evolution of phase transformation fronts and associated thermal effects in a NiTi tube under a biaxial stress state. Extreme Mech. Lett. 8, 55–63.
Brazier, L.G., 1927. On the flexure of thin cylindrical shells and other thin sections. Proc. R. Soc. Lond. A 116, 104–114.

Ericksen, J.L., 1975. Equilibrium of bars. J. Elast. 5, 191–201.
Gall, K., Sehitoglu, H., Chumlyakov, Y.I., Kireeva, I.V., 1999. Tension-compression asymmetry of the stress-strain response in aged single crystals and polycrystalline NiTi. Acta Mater. 47, 1203–1217.
Gall, K., Sehitoglu, H., 1999. The role of texture in tension-compression asymmetry in polycrystalline NiTi. Int. J. Plast. 15, 69–92.
Hallai, J.F., Kyriakides, S., 2011a. On the effect of Lüders bands on the bending of steel tubes: part I experiments. Int. J. Solids Struct. 48, 3275–3284.
Hallai, J.F., Kyriakides, S., 2011b. On the effect of Lüders bands on the bending of steel tubes: part II analysis. Int. J. Solids Struct. 48, 3285–3294.
Hallai, J.F., Kyriakides, S., 2013. Underlying material response for Lüders-like instabilities. Int. J. Plast. 47, 1–12.
Jacobus, K., Sehitoglu, H., Balzer, M., 1996. Effect of stress state on the stress-induced martensitic transformation of polycrystalline Ni-Ti alloy. Metall. Mater. Trans. A 27, 3066–3073.
Jiang, D., Bechle, N.J., Landis, C.M., Kyriakides, S., 2016a. Buckling and recovery of Niti tubes under axial compression. Int. J. Solids Struct. 80, 52–63.
Jiang, D., Landis, C.M., Kyriakides, S., 2016b. Effects of tension/compression asymmetry on the buckling and recovery of NiTi tubes under axial compression. Int. J. Solids Struct. 100–101, 41–53.
Jiang, D., Landis, C.M., 2016. A constitutive model for isothermal pseudoelasticity coupled with plasticity. Shape Mem. Superelast. 2, 360–370.
Jiang, D., Kyriakides, S., Landis, C.M., Kazinakis, K., 2017a. Modeling of propagation of phase transformation fronts in NiTi under uniaxial tension. Eur. J. Mech. A/Solids 64, 131–142.
Jiang, D., Kyriakides, S., Bechle, N.J., Landis, C.M., 2017b. Bending of pseudoelastic NiTi tubes. Int. J. Solids Struct. 124, 192–214.
Kyriakides, S., Ju, G., 1992. Bifurcation and localization instabilities in cylindrical shells under bending—I. Experiments. Int. J. Solids Struct. 29, 1117–1142.
Ju, G., Kyriakides, S., 1992. Bifurcation and localization instabilities in cylindrical shells under bending—II. Predictions. Int. J. Solids Struct. 29, 1143–1171.
Kyriakides, S., Miller, J.E., 2000. On the propagation of Lüders bands in steel strips. ASME J. Appl. Mech. 67, 645–654.
Li, Z.Q., Sun, Q.P., 2002. The initiation and growth of macroscopic martensite band in nano-grained NiTi microtube under tension. Int. J. Plast. 18, 1481–1498.
Mao, S.C., Luo, J.F., Zhang, Z., Wu, M.H., Liu, Y., Han, X.D., 2010. EBSD studies of the stress-induced B2-B19′ martensitic transformation in NiTi tubes under uniaxial tension and compression. Acta Mater. 58, 3357–3366.
Needleman, A., 1988. Material rate dependence and mesh sensitivity in localization problems. Comp. Methods Appl. Mech. Eng. 67, 69–85.
Reedlunn, B., Churchill, C.B., Nelson, E.E., Shaw, J.A., Daly, S.H., 2014. Tension, compression, and bending of superelastic shape memory tubes. J. Mech. Phys. Solids 63, 506–537.
Sedlak, P., Frost, M., Benešova, B., Ben Zineb, T., Šittner, P., 2012. Thermomechanical model for NiTi-based shape memory alloys including R-phase and material anisotropy under multi-axial loadings. Int. J. Plast. 39, 132–151.
Shaw, J.A., Kyriakides, S., 1995. Thermomechanical aspects of NiTi. J. Mech. Phys. Solids 43, 1243–1281.
Shaw, J.A., Kyriakides, S., 1997. On the nucleation and propagation of phase transformation fronts in a NiTi alloy. Acta Mater. 45, 683–700.
Watkins, R.T., Reedlunn, B., Daly, S., Shaw, J.A., 2018. Uniaxial, pure bending, and column buckling experiments on superelastic NiTi rods and tubes. Int. J. Solids Struct. 45, 3074–3087.